J Mater Sci (2022) 57:21020–21038

Chemical routes to materials

Molecular dynamics of epoxy nanocomposites filled with core–shell and hollow nanosilica architectures

Sunny Chaudhary[1,*], Orestis Vryonis[1], Alun Vaughan[1], and Thomas Andritsch[1]

[1] Tony Davies High Voltage Laboratory, Department of Electronics and Computer Science, Faculty of Engineering and Physical Sciences, University of Southampton, University Road, Southampton SO17 1BJ, Hampshire, UK

Received: 24 March 2022
Accepted: 4 November 2022

ABSTRACT

Here we contrast the molecular dynamics of epoxy nanocomposites filled with three different types of silica-based nanoparticles with different architectures, namely solid core, core–shell and hollow and with varying degree of crystallinity. The samples are characterised by Fourier transform infrared spectroscopy, differential scanning calorimetry, broadband dielectric spectroscopy and dynamic mechanical analysis (DMA). Widely known relaxations such as α, β, γ, normal mode and interfacial polarisation are observed and discussed. An additional relaxation named omega (ω) is also observed, whose dielectric strength is inversely correlated to the crystallinity of the nanoparticles. We suggest that this may be attributed to the polarizing interaction of the hydroxyl groups of silanols with the hydroxy ether groups of the polymer chain. The ω is absent in DMA confirming it as a polarisation phenomenon. At lower concentration of silanols, the ω largely overlaps with β, effectively becoming an integral part of it. Finally, two interfacial polarisation relaxations are observed in the case of core–shell structures, originating from the core–shell and shell–polymer interface but, due to the similar real permittivity values of the core, shell and the polymer, their dielectric strength is weak.

Introduction

Many studies have reported substantial improvements in the thermal [1], mechanical [2] and electrical properties [3] of epoxy-based systems as a result of the judicious addition of nanoparticles. The origin of these effects has been explored by investigating different factors, such as filler size and shape [4], concentration [5], chemical structure [6], synthesis method and surface modifications [7], and is commonly attributed to interfacial phenomena, molecular

---

Handling Editor: Yaroslava Yingling.

Address correspondence to E-mail: sc6u16@ecs.soton.ac.uk

Springer

https://doi.org/10.1007/s10853-022-07938-7

dynamics, or both. Consequently, various hypotheses have been proposed, including the intensity model [8], the interphase volume model [9], the multicore model [10] and loosely–tightly bound layer model [11], which commonly explain the above effects in terms of the formation of a local interaction zone within the polymer as a result of interfacial interactions. However, most of these ideas do not consider the architecture of the nanoparticles and treat the nanoparticles as isotropic and homogeneous and consequentially, and much emphasis has been given to the polymer–shell (p–s interface) and matrix–nanoparticle interactions, that is, to processes *adjacent to* the nanoparticles. Conversely, relatively less attention has been focused on processes *within* nanoparticles. Specifically, in the case of core–shell nanoparticles, the effect of the interface between core and shell (c–s interface) is sparsely studied.

Despite many studies reporting enhanced nanocomposite properties, numerous other published studies have described contrary results. Consider, for example, the effect of nanotitania (TiO_2), which has been considered in earlier studies [12]. Singha et al. investigated the dielectric properties of epoxy-based nanocomposites containing 10 wt% of a TiO_2 filler. That work reported that the real part of the relative permittivity (ε') at frequencies lower than 10^3 Hz for this system was *higher* than unfilled epoxy, an effect that was attributed to the dominant role played by this high permittivity filler. Elsewhere Nelson and Fothergill [13] reported contrary results for a similar system and filler loading level; in this case, ε' of the epoxy nanocomposite is reported to be *lower* than that of the unfilled epoxy. This behaviour is attributed to the restriction of end-chain and side-chain movement of the polymer due to the addition of the fillers. A possible explanation for this inconsistency is that different interfacial areas are formed in the two systems, even at the same weight percentage, since different nanoparticle systems will generally differ in size, specific surface area, structure, etc. Thus, when polymers are filled with nanoparticles based on volume or weight percentage, the interfacial areas that form may, nevertheless, be significantly different. Since interfaces play a vital role in bulk nanocomposite properties, it is crucial to adopt a controlled approach when seeking to develop a sound understanding of the role of interfacial processes. Due to the complexity of molecular dynamics, understanding the underlying mechanisms is challenging even for an unfilled epoxy system—this complexity is further enhanced by the addition of fillers.

In this paper, we report on the molecular dynamics of epoxy nanocomposite systems filled with three different nanoparticles, while maintaining a similar interfacial surface area: silica (SiO_2), referred to as "core" only; core–shell silica–silica (SiO_2–SiO_2) and hollow silica (h-SiO_2). Further, the degree of crystallinity is different for different nanoparticle architecture, SiO_2 is calcined and therefore crystalline [14], SiO_2–SiO_2 has a crystalline core similar to SiO_2 but the shell is amorphous, whereas h-SiO_2 is entirely amorphous. The primary focus is to investigate the origins of observed dielectric phenomena occurring both within the bulk of the matrix, in the polymeric shell surrounding each nanoparticle and additional interfacial phenomena originating from the core–shell interfaces present within relevant systems.

Experimental

Materials

A diglycidyl ether of bisphenol A-type epoxy resin (DER 332) was obtained from Sigma-Aldrich (epoxide equivalent molar mass 172–176 g mol^{-1}), and the amine hardener Jeffamine D-230 was obtained from Huntsman (hydrogen equivalent mass of 60 g mol^{-1}). A constant stoichiometry was used throughout, namely 1000:344 parts (resin: hardener). Silica (SiO_2) nanoparticles with a specific surface area of 590–690 m^2 g^{-1} equating to a size 5–20 nm (diameter) were obtained from Sigma-Aldrich and used directly and for the production of core–shell structures. The reagents used for the synthesis of core–shell and hollow silica (h-SiO_2) nanoparticles, namely tetraethyl orthosilicate ($\geq$ 90%, TEOS), hexadecyltrimethylammonium bromide (CTAB), ammonium oxide andpoly (acrylic acid sodium salt) (PAA—Na, M.W. ~ 5100 g mol^{-1}), were also obtained from Sigma-Aldrich.

Sample preparation

Core–shell nanoparticles (SiO_2–SiO_2) and hollow nanoparticles (h-SiO_2) were synthesised using the Stöber method [15]. In this, 3 g of CTAB was dissolved in 300 ml of deionized water and stirred to form a homogeneous solution. Separately, 2.5 g of SiO_2 was dispersed in 200 ml of deionised water and continuously stirred for 6 h using a magnetic stirrer before being probe sonicated (UP 200S) for 1 h to break up any agglomerates. The CTAB solution was then added to the aqueous nanosilica dispersion, mixed and stirred for 24 h at 20 °C to ensure complete CTAB film formation on the nanoparticles' surface. The resulting suspension was then centrifuged at 8000 rpm for 10 min (Heraeus Megafuse 8 centrifuge) to precipitate the CTAB-coated silica, and the supernatant liquid containing unabsorbed CTAB was removed. The nanoparticles were next re-dispersed in deionised water, and the washing process repeated three times before, finally, being dispersed in a mixture of 100 ml deionised water and 400 ml ethanol. To this suspension, 5 ml of aqueous ammonia was added and stirred for 2 min, after which 5 ml of TEOS was added to the solution. This mixture was stirred for 16 h at 20 °C, followed by one centrifugation washing cycle with ethanol and two with deionised water. Finally, the obtained particulate was vacuum-dried at 60 °C for 12 h to obtain core–shell SiO_2–SiO_2 nanoparticles.

A similar process was used to synthesise the hollow structures, but using PAA-Na to form template particles [16–18]. 0.09 g of PAA-Na powder (molar mass ~ 5100 g mol^{-1}) and 25% ammonia solution were mixed using a magnetic stirrer until completely dissolved. Then 30 ml of ethanol was then added to the solution and stirred for 2 h. Further, 0.15 ml of TEOS was added, followed by stirring for a total reaction time of 16 h. The suspensions were then washed with ethanol and deionised water, centrifuged and dried at 60 °C for 12 h to obtain h-SiO_2 nanoparticles.

All the samples used here (nanocomposite and unfilled systems) were prepared using the same standard solvent method. First, the resin was heated at 50 °C for at least 1 h to reduce its viscosity before it was added to acetone and stirred for 1 h. Separately, the required mass of nanoparticles was dispersed in acetone at a loading level of 5 mg/mL, the mixture was stirred for 2 h, and then probe sonicated for 60 min. The nanoparticle dispersion and the epoxy/acetone solution were then mixed and stirred for 2 h, before the solvent was removed, initially, using a rotary evaporator and, then, by placing the product in a vacuum oven for 12 h at 20 °C. Finally, the epoxy/nanoparticle system was heated to 50 °C, with stirring, and weighed periodically to ensure maximal removal of solvent. When no further mass loss was detected, the hardener was added to the epoxy/nanoparticle mixture, stirred for 20 min and degassed for 20 min before, finally, being introduced into moulds of the required dimensions. Samples were cured at 80 °C for 2 h and then post-cured at 125 °C for 3 h before being left in the oven to cool to room temperature, in accordance with following the manufactures recommendation and prior study [19]. From the resulting sheets, specimens 200 µm in thickness were selected for study. The samples were then stored under vacuum inside a desiccator until further use. For all nanocomposites, the loading ratio of nanoparticles was chosen such that the total interfacial area with the host polymer would be comparable, regardless of the different silica structures, as described elsewhere [20].

Table 1 provides information regarding the average sample size, particle weight used, the corresponding weight percentage and the density of the different nanoparticles for the three selected surface areas of 1.16 m^2, 5.80 m^2 and 11.6 m^2. Furthermore, it can be observed in Table 1 that the thickness of the shell in case of h-SiO_2 in the present study is noticeably higher than that in the literature, potentially due to the following reasons:

(a) The molecular weight used in the reference for poly acrylic acid (PAA) is 5000. In present study, this is slightly higher, i.e. ~ 5100. Following the exact procedure as presented in the reference led to a high concentration of nanoparticles with incomplete shell formation. During the centrifuge process with low concentration of ammonia, the shell collapsed due to mechanical strain. One of the factors to dominate the shell thickness is the concentration of ammonia. It can be varied to control the thickness of the shell from several tens to hundreds nm [17]. Therefore, the amount ammonia, which acts as a nucleating agent, was varied to get complete formation of the shells and has better mechanical stability; hence, a higher molar ratio of ammonia was used.

(b) Secondly, the stirring time in the reference is a maximum of 14 h; however, in the present study the mixture was stirred for 16 h which

Table 1 Calculated values for the weight percentage to maintain the same surface area across all samples based on the nanoparticle average size and their density

Sample	Weight percentage (wt%)	Particle weight (mg)	Density (g/cm^3)	Average size (nm)	Surface area (m^2)
SiO_2—1	0.03	2.98	2.2	15 (5–20)	1.16
SiO_2—5	0.15	14.9			5.80
SiO_2—10	0.30	29.8			11.6
SiO_2–SiO_2—1	0.20	14.21	2.1	35 (30–45)	1.16
SiO_2–SiO_2—5	1	71.05			5.80
SiO_2–SiO_2—10	2	142.1			5.80
h-SiO_2—1	0.21	15.31	1.32	60 (57–72)	1.16
h-SiO_2—5	1.05	76.5			5.80
h-SiO_2—10	2.1	153.1			11.6

lead to higher deposition of SiO_2 from the TEOS forming a thicker and stable shell.

In a prior study, it was demonstrated that even after careful preparation ~ 1% of h-SiO_2 nanoparticle still had incomplete shell formation [21].

Methodology

Transmission electron microscopy (TEM) was conducted using a Hitachi H 7000 TEM operated under high-resolution bright-field mode. To prepare the required samples, a quantity of nanoparticles was added to ethanol and sonicated and a small drop of the resulting dispersion placed onto a carbon-coated TEM grid. To determine the particle size distribution present in a given system, multiple TEM images were obtained from different areas of the above grids, with 40 nanoparticles being chosen at random from these multiple images for analysis using the ImageJ image analysis software package. Attenuated total reflection Fourier transform infrared (ATR-FTIR) spectra were obtained using an iD7 Nicolet iS5 spectrometer from ThermoFisher. All the epoxy nanocomposites data shown were baseline-corrected and normalised using the 1509 cm^{-1} absorbance peak [22]. In case of powder nanoparticles, the normalisation was done on a 0–1 basis. A Mettler Toledo DSC820 differential scanning calorimetry (DSC) was used to evaluate glass transition temperatures (T_g) after calibration of the instrument using high-purity indium, as well as zinc. In all cases, a ~ 4.5 mg in mass was employed using a two-step heating cycle, where the first cycle was used to erase the thermal history of the sample and the second cycle was used to determine the reported T_g, which was taken as the inflexion point in the heat flow curve. Throughout the heating/cooling/heating programme, a constant rate of 10 °C min^{-1} was used. Three samples were measured per material; the T_g was calculated by the mean value and the experimental uncertainty by standard deviation. The dielectric response of the samples was measured via broadband dielectric spectroscopy (BDS) using a Solartron 1296 dielectric interface and a Schlumberger SI 1260 impedance/phase gain analyser. Samples were sputter-coated with 20-mm-diameter gold electrodes prior to analysis and then mounted in a Janis Research STVP 200 XG system for measurement over the temperature range of − 160 to 160 °C. An AC voltage of 7 V was used from 10^{-1} to 10^5 Hz; an integration time of 10 s was used above 1 Hz; below 1 Hz acquired data were averaged over 10 cycles. A Mettler Toledo DMA/SDTA861 was used for dynamic mechanical analysis (DMA). It was operated in tension mode with a maximum force of 10 N or 3 µm maximum level with an auto offset of 150%. Measurements were carried out in isothermal steps of 10 °C for a temperature range of − 100 °C to 160 °C and a frequency sweep of 10^{-3} to 100 Hz.

Result and discussion

Transmission electron microscopy

Figure 1 shows TEM images obtained for the three different types of nanoparticles, i.e. SiO_2 (Fig. 1a) and SiO_2–SiO_2 core–shell nanoparticles (Fig. 1b) and h-SiO2 hollow nanoparticles (Fig. 1c). In the case of the SiO_2–SiO_2 core–shell nanoparticles, no clear contrast is evident between the core and the shell, since

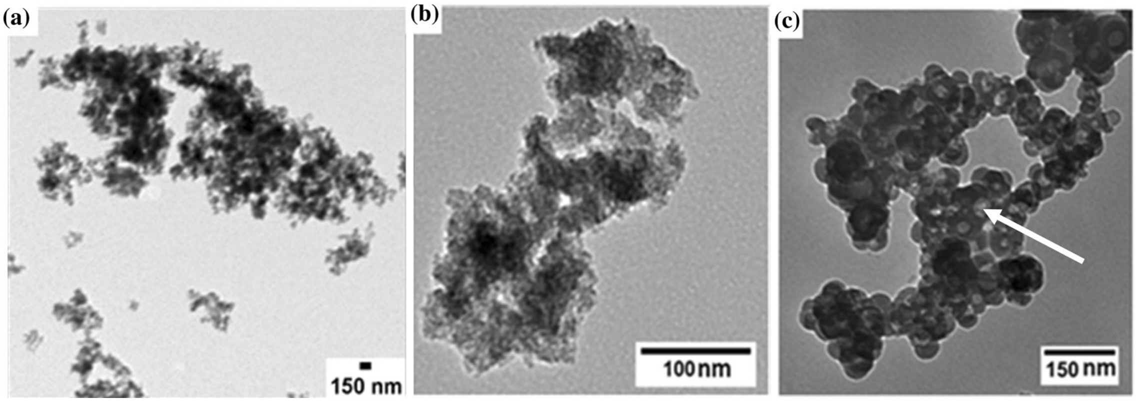

Figure 1 Transmission electron microscopy images of different nanoparticle architecture types **a** SiO_2, **b** SiO_2–SiO_2 (core–shell), **c** h-SiO_2 (hollow).

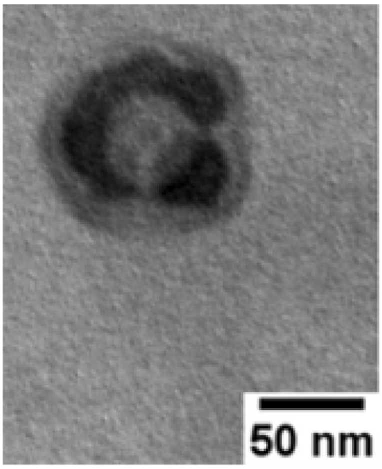

Figure 2 TEM micrograph showing an isolated h-SiO_2 nanoparticle with an incomplete shell.

the material is equivalent in both regions. Conversely, in Fig. 1c, a distinct contrast between the core and the shell can be observed, due to the hollow core, leading to structures composed of a darker circular region surrounding a lighter central core (example arrowed). An example of such a structure but where the formation of the SiO_2 shell appears incomplete is shown in Fig. 2. Only few nanoparticles with incomplete structures were found as such we assume that the effect of this on the particle surface area is negligible. This may be a result of shell collapse due to mechanical weakness [23] or inadequate deposition of SiO_2 on the PAA-Na template. Nevertheless, in this image, three different grey levels are evident corresponding to the carbon support film (lightest region); the h-SiO2 shell (darkest, approximately annular region); intermediate grey level, corresponding to transmission via the hollow nanoparticle core and periphery. While the precise details of the contrast will depend the nanoparticle geometry, the general appearance evident in Figs. 1c and 2 is consistent with thickness contrast arising from a hollow structure deposited on a support film. The median nanoparticle size and their size distribution are presented in Fig. 3. For SiO_2–SiO_2, the average nanoparticle size is ~ 35 nm, but with a sizable fraction of the distribution falling within broader size range of ~ 25–45 nm, as illustrated in Fig. 3a. This size variation has been accounted for when calculating the nanoparticle loading level required to maintain a comparable similar interfacial area in all the systems studied. The size of the SiO_2 nanoparticles quoted by the manufacturer is ~ 5–20 nm, with an average size of ~ 10 nm, implying that the chemical treatment used to produce the SiO_2–SiO_2 resulted in a shell 20–25 nm in thickness. For h-SiO_2, the average nanoparticle size is ~ 60 nm, and the average pore size is ~ 30 nm, leading to the conclusion that, in this case, the shell is ~ 15 nm thick.

Fourier transform infrared spectroscopy

Nanoparticle powders

In their idealised crystalline form, silica (SiO_2) nanoparticles contain, in terms of mass percentage, 46.63% silicon and 53.33% oxygen [24], arranged with tetrahedral coordination [25]. Deviations from this coordination increase the ionic character of the constituent Si–O bonds and lead to microstructural differences and an amorphous structure [26]. Since there are no peaks which can be used as reference, where the concentration of the involved groups is constant

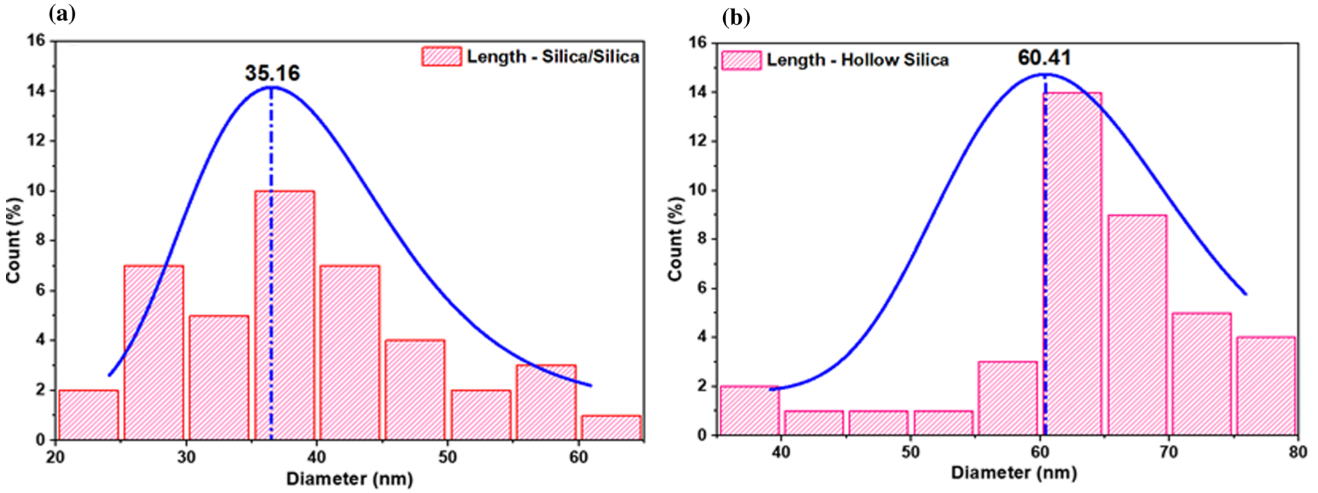

Figure 3 Illustration of the nanoparticle size distribution number count percentage, distribution curve and the average nanoparticle size, obtained after image analysis of TEM graphs of the two synthesised nanoparticle architecture types i.e. **a** SiO_2–SiO_2 (core–shell), **b** h-SiO_2 (hollow).

across all systems, normalising the FTIR data of the nanoparticles would be complex and inaccurate. Therefore, the data were only baseline-corrected. However, acknowledging this, to achieve certain level of comparability between these samples, the amount of nanoparticle by weight homogenously spread onto the crystal was kept the same at 4 mg. Measured FTIR spectra of the three nanoparticle types measured in their powder form are presented in Fig. 4a; consider, first, the four absorption peaks at ~ 1170 cm^{-1}, 1100–1068 cm^{-1}, 950 cm^{-1} and 800 cm^{-1}, all of which are related to the vibrations of Si–O–Si. The dominant peak spanning 1100–1068 cm^{-1} is attributed to the asymmetric stretching (ν_{as}) of the Si–O–Si bonds in the SiO_4 tetrahedron structure in transversal optical (ν_{as}–TO) mode, while the shoulder at ~ 1170 cm^{-1} arises from asymmetric Si–O–Si bond stretching (Si–O–Si ν_{as}–LO) in the longitudinal optic mode [27]. For the same weight of these nanoparticles, significant variation in the concentration of the Si–O–Si bonds is observed. From Fig. 4a, it is evident that the position of the TO absorbance peak varies from system to system, being located at 1100 cm^{-1} in the core SiO_2 nanoparticles, at 1084 cm^{-1} in the SiO_2–SiO_2 core–shell system and at 1068 cm^{-1} in the h-SiO_2 nanoparticles. Such variations in the position of this spectral peak are a consequence of changes in local ordering and variations in bonding character [28–35]. Specifically, the data presented in Fig. 4a indicate increased degrees of disorder in the core–shell and hollow nanoparticles compared with core SiO_2 system.

Consider, now, the absorbance around 950 cm^{-1}, which stems from the silanol (Si–OH) groups present in each nanoparticle system [36]. From Fig. 4a, it is observed that absorbance in this spectral region is lowest for SiO_2 and highest for h-SiO_2. However, the concentration of –OH group for SiO_2–SiO_2 is inconclusive due to the inverted absorbance peak. This inverted peak is still visible after several reruns and is assumed to be the consequence of an equipment error. However, other peaks' reported trends or behaviours are not significantly influenced when similar percentages of error are taken into account. Nevertheless, certain inferences can be drawn by analysing the knows simultaneously to establish a trend. Firstly, SiO_2 has the highest density followed by SiO_2–SiO_2 and h-SiO_2. Therefore, SiO_2 should ideal have the highest concentration of ordered Si–O–Si bonds. This is further evidenced by the fact that SiO_2 is calcined at 800 °C (as received from the manufacturer), whereas the synthesised nanoparticles were only vacuum dried at 60 °C. Higher-temperature treatment leads to further condensation and formation of silanol bridges. Secondly, even though the surface area of the nanoparticles is theoretically the same, the volume is significantly different. Volume of SiO_2 shell in SiO_2–SiO_2 is ~ 30 mm^3 and for h-SiO_2 is ~ 49 mm^3. The temperature treatment in both the case is the same. A similar condensation rate would lead to higher concentration of Si–OH bonds

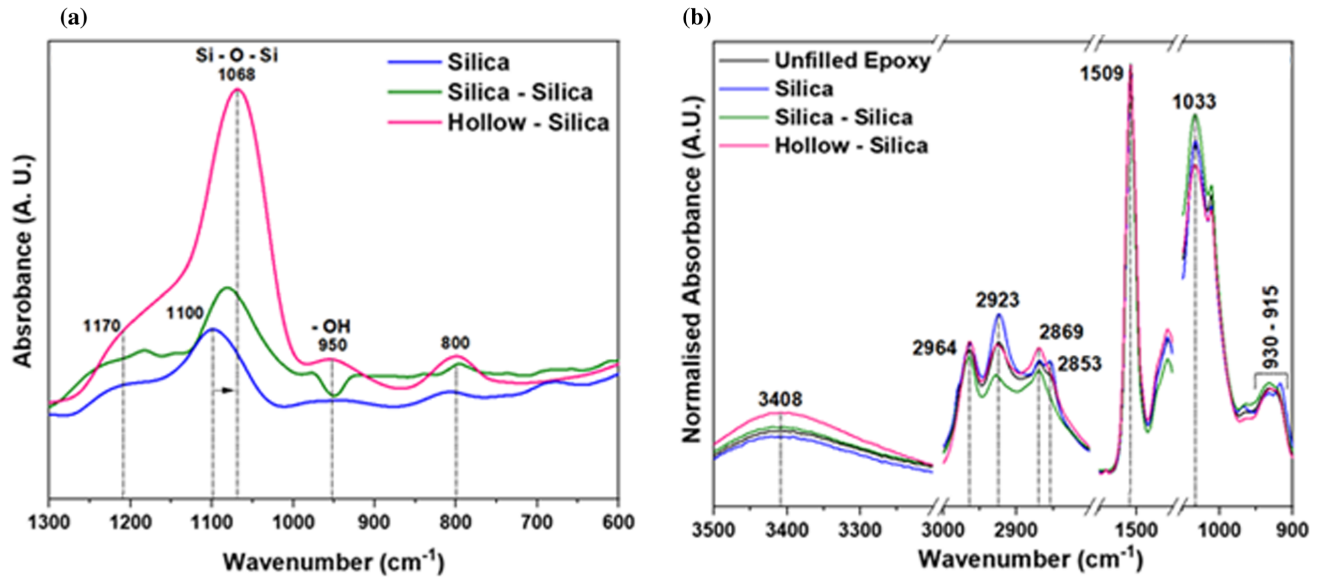

Figure 4 **a** FTIR spectra of the nanoparticle powders presented for the three different nanoparticle types, namely SiO_2 (core), SiO_2–SiO_2 (core–shell) and h-SiO_2 (hollow) in the 1300–600 cm^{-1} wavenumber range. **b** FTIR spectra of reference unfilled epoxy system along with the epoxy nanocomposite systems, filled with SiO_2, SiO_2–SiO_2 and h-SiO_2 nanoparticles. Illustrating the absorbance peaks in five different regions, i.e. 3500–3200 cm^{-1} (hydroxyl), 3000–2800 cm^{-1} (hydrocarbon stretching), 1550–1450 cm^{-1} (aromatic–calibration peak), 1050–1000 cm^{-1} (diethylene ether) and 1000–900 cm^{-1} (epoxide ring vibration) starting from high wavenumber towards lower.

remaining in h-SiO_2 as compared to SiO_2–SiO_2 due to this difference in shell volume. It is expected that some of these Si–OH would be present on the internal surface of the h-SiO_2; however, due to a small pore size (30 nm) leading to steric hindrance, majority are likely to be either in the volume or on the external surface. Therefore, as compared to SiO_2–SiO_2 is likely that the concentration of Si–OH on the surface of h-SiO_2 is higher. That is, the concentration of silanol groups increases with increasing structural disorder. This suggests that silanol groups are not only present at surfaces, but also within the bulk of the nanoparticles and are related to structural defects, albeit that in the case of the hollow nanoparticles, the additional internal surface is a further contributory factor. For example, if one Si atom in a tetrahedral SiO_4 unit were missing, then four silanol groups would be required to maintain the stoichiometry, being hydrogen-bonded to form a so-called silanol nest [37]. Furthermore, disordered SiO_2 networks may also contain SiO_x–Si–$(OH)_y$ groups, where the sum of x and y is equal to 4 and $x \geq 1$. Such defects have been ascribed to incomplete dehydration or the lack of an available adjacent Si bonding site [37, 38] Nevertheless, the previous assertion of increased disorder in the core–shell and hollow nanoparticles is supported by the increased silanol absorption seen in these systems.

The absorbance band intensity is directly proportional to the respective functional group concentration [39]. However, h-SiO_2 nanoparticles with the lowest density and the least concentration of Si–O–Si bonds have the strongest absorbance peak; this is attributed to the presence of the mentioned hydrogen bonds. The higher the concentration of these hydroxyl groups (Si–OH), the greater the possibility of forming hydrogen-bonded bridges, leading to noticeable shifts and an increase in the intensity of Si–O–Si absorbance bands. SiO_2–SiO_2 and h-SiO_2 underwent a similar drying procedure, yet h-SiO_2 has a higher hydroxyl group concentration; this is likely due to either lack of higher drying temperature or the additional internal surface area where surface Si–OH could exist. Hence, h-SiO_2 with the lowest density, highest OH and Si–O–Si (v_{as}–LO) peak intensities, lowest wavenumber peak location for Si–O–Si (v_{as}–TO) represent a highly amorphous structure and the strongest influence of hydrogen bonding followed by SiO_2–SiO_2. Finally, the absorbance band at 800 cm^{-1} is attributed to the symmetric stretching vibration (v_s) of Si–O bonds [40]. Figure 5 gives an approximate visual perception of the different architecture of the

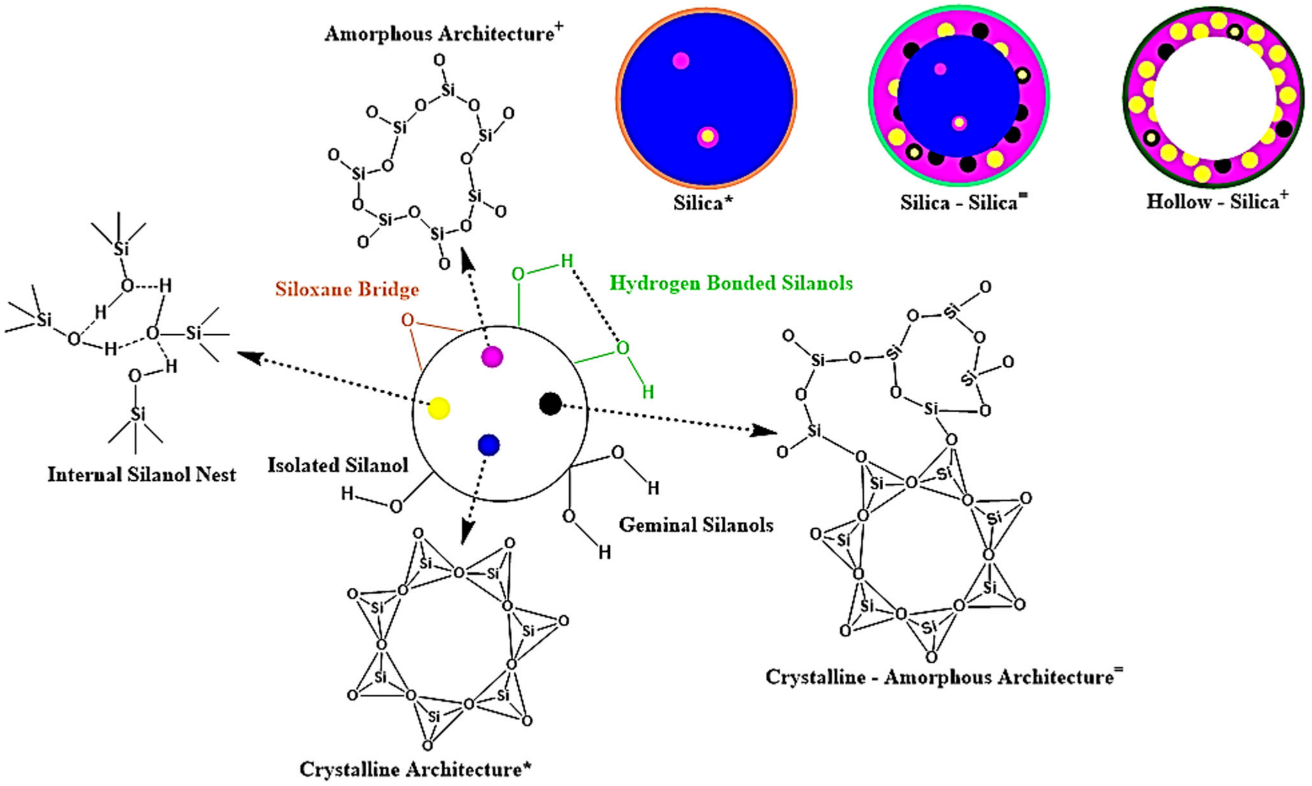

Figure 5 Illustration of different silanol groups that could be present on the nanoparticle surface i.e. **a** Isolated, **b** geminal and **c** hydrogen bonded. Due to condensation during calcination these groups form siloxane bridges on the surface of the nanoparticle. Internally, the nanoparticle could be either **a** amorphous, **b** crystalline or **c** a combination of both amorphous and crystalline depending upon the heat treatment. Without condensation at sufficiently high temperature not all silicic acid molecules dehydrate and form the networked crystalline structure which introduces defects in form of silanol nests. The diagram of nanoparticle architecture in the top right corner approximately represents the concentration and combination of defects along with the varying level of crystallinity of the nanoparticles used in this study.

nanoparticles, concentration of the silanol nests and the varying crystallinity of the nanoparticles.

Unfilled epoxy and epoxy nanocomposites

FTIR data obtained from the reference unfilled epoxy and related nanocomposites filled with 10 rel. wt% (11.6 m^2) are presented in Fig. 4b. In these spectra, the absorbance band at 1509 cm^{-1} is attributed to the stretching vibration of aromatic carbons, the concentration of which is known in all samples. As such, this absorbance band was used as an internal calibrant to scale the spectra, as described elsewhere [41, 42]. These spectra are consistent with published data obtained from comparable materials whereby the absorbance bands at $\sim$ 3408 cm^{-1} and $\sim$ 1033 cm^{-1} can be attributed to hydroxyl and ether groups [43, 44].

The differences in the intensity of the absorbance band for ether groups are due to the contribution from the Si–O–Si (ν_{as}–TO). Unlike the h-SiO_2-filled epoxy, the Si–O–Si (ν_{as}–TO) does not contribute to the ether absorbance band in the unfilled epoxy sample. Given the constant optimal stoichiometric ratio maintained across all samples, the minimum concentration of ether groups in h-SiO_2 filled sample should be similar to unfilled epoxy, which is not observed. Therefore, the noticeable difference in the intensity could also be due to a difference in ether concentration from changes in curing kinetics (which is not the case with referring to the DSC data below).

Noticeably higher intensity of hydroxyl absorbance band ($\sim$ 3408 cm^{-1}) is observed compared to other samples for h-SiO_2 filled sample. Ideally, these hydroxyl groups are produced during the curing reaction (E_{OH}). However, the increase in intensity could also be due to an overlapping band which is attributed to the stretching vibration contributions from the hydroxyl groups (Si_{OH}) of the silanols

(ν_{SiOH}-isolated, terminal and geminal) and their interfacial interactions with the hydroxyl groups of other functional groups [40, 45]. ν_{SiOH} was not observed in the spectra of any nanopowder. Hence, the absorbance band is most likely originating from the interfacial interaction of Si_{OH} and E_{OH}. The two absorbance peaks of the hydroxyl groups: one from curing and the other from silanols, cannot be easily deconvoluted without knowing their specific concentration. Therefore, a hard conclusion cannot be drawn. This notion will be further analysed in the following section in terms of glass transition temperature (T_g).

Even in stoichiometrically balanced systems, about 1–2% of epoxides remain unreacted due to steric hindrance [46]. The weak 930–915 cm^{-1} absorbance region is attributed to their ring vibrations [47], where no significant changes are observed, which complies with the balanced stoichiometry of those samples.

Significant changes in the intensity of absorbance bands related to the stretching vibrations of CH_3 groups (2964—υ_{as} and 2869—υ_s) can also be observed in case of SiO_2 and SiO_2–SiO_2. Residual TEOS or CTAB as micelles formation could affect their concentration. However, no such peaks were observed in the nanopowder spectra neither for CH_2 nor CH_3 (2800–3000 cm^{-1}), confirming the complete removal of unreacted TEOS and adsorbed CTAB. Therefore, observed variations are potentially due to the change in the dipole moment of CH_3 of the epoxy resin due to the addition of nanofillers; this requires further investigation in the framework of a separate study.

Differential scanning calorimetry

The glass transition is related to long-chain motions of the polymer, a transition from a rigid glassy state to a rubbery state, and is commonly related to the dielectric alpha (α) relaxation [48]. Figure 6 presents DSC T_g values for the unfilled epoxy and epoxy nanocomposite samples filled with three different total surface area-based loading levels. The mean T_g of the reference unfilled epoxy is 84 °C, in line with published literature [49]. The mean T_g for all the epoxy nanocomposite samples, irrespective of the loading level, lies in the range of 81–86 °C. These variations are minor and are commensurate with the experimental uncertainties (standard deviation–error bar), with the implication that within the composition range considered here, neither the loading level nor the nanoparticle architecture significantly affects the measured T_g.

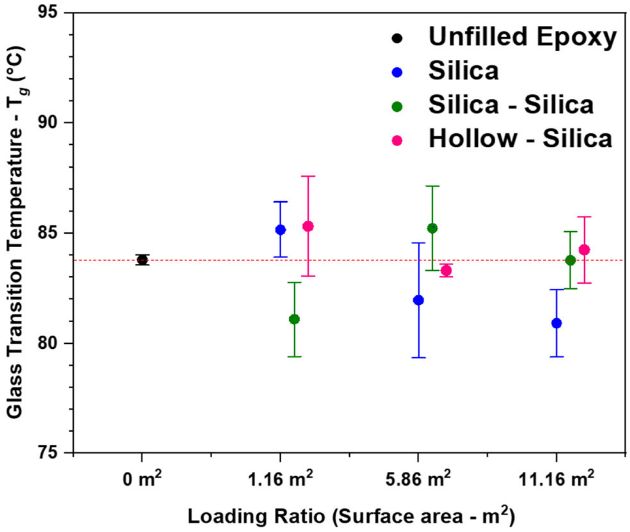

Figure 6 Glass transition temperature of unfilled epoxy along with three different total surface area loading ratio for **a** SiO_2, **b** SiO_2–SiO_2 and **c** h-SiO_2 epoxy nanocomposites.

The T_g is a function of many parameters; the degree of cross-linking is one of the parameters which correlates well, in direct proportion [50, 51]. As the T_g does not vary between samples, it can be inferred that their degree of cross-linking is also similar. Referring to the FTIR spectra, the increase in hydroxy ether band intensity is therefore justifiably due to the overlapping band and not cause of increased cross-linking.

Broadband dielectric spectroscopy

Dielectric spectroscopy is a widely used method to study polarisation behaviour, molecular dynamics and the effect of the electric stimulus on nanocomposite systems. The complex dielectric permittivity can be written as follows: $\varepsilon^* = \varepsilon' - i\varepsilon'$, where ε' is the real part and ε'' represents the imaginary part of the complex permittivity [22]. Dielectric spectra are generally a superposition of different relaxation and dispersion phenomena. Under an applied AC field, changes in the polarisation behaviour of the system and the composing polar groups alter the ε' and ε'' spectra. These alterations could be associated with different relaxations such as the alpha (α), beta (β), gamma (γ) and interfacial polarisation phenomena.

In order to separate the dielectric phenomena from the ionic conduction or low-frequency dispersion, a first-order approximation of the Kramers–Kronig relation was used, described by the following equation [52]:

$$\varepsilon''_{\mathrm{derived}} = -\frac{\pi}{2}\frac{\partial \varepsilon'(\omega)}{\partial \log \omega} \approx \varepsilon'' \tag{1}$$

Equation 1 approximately converts the real part of the permittivity ε' into the imaginary part ε'', eliminating the direct current conduction contributions. Figure 7 shows the variation of ε' (Fig. 7a, c) and $\varepsilon''_{\mathrm{derived}}$ (Fig. 7b, d) with respect to temperature at 1 Hz and 10 Hz. These frequencies show all the observed phenomena and relaxations for the reference unfilled epoxy and all the filled samples. These plots give an overview of the following sections where all the phenomena are discussed in detail. As expected, with an increase in the frequency the respective relaxations shift towards higher temperature. The alpha (α), beta (β) and gamma (γ) are common across all the plots in both ε' and $\varepsilon''_{\mathrm{derived}}$, visible distinctly. Similarly, the normal mode (n-mode) relaxation and interfacial polarisation phenomena are also observed in all the plots; except in Fig. 7d where the interfacial polarisation peaks have moved out of the measured temperature range (towards higher temperature). The gamma (γ) relaxation can be observed in the $\varepsilon''_{\mathrm{derived}}$ plots towards the lower temperatures (− 160 to − 130 °C). Moreover, the filled epoxy systems display an additional relaxation located between the α and the β modes with varying intensity that inversely aligns with the degree of silica surface crystallinity.

To quantify the relaxation characteristics and study the effect of nanoparticle architecture and concentration on the molecular dynamics of epoxy nanocomposite systems, an empirical Havriliak–

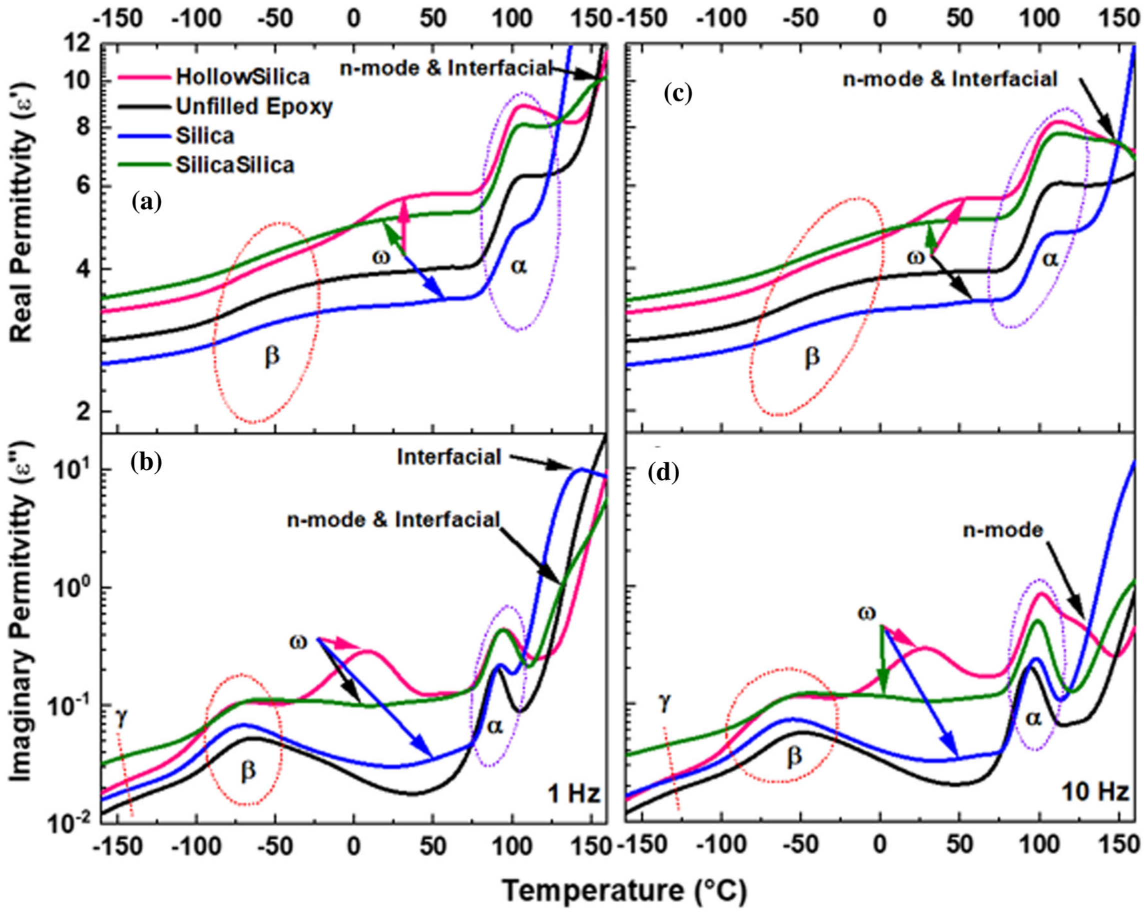

Figure 7 ε' (**a** and **c**) and ε''-derived (**b** and **d**) dielectric spectra for unfilled epoxy and all the filled epoxy systems at **a** 1 Hz, **b** 100 Hz for a temperature range of − 160 to 160 °C presenting the gamma (γ), beta (β), omega (ω), alpha (α), normal (n) mode relaxations and interfacial polarisation phenomena.

Negami (HN) formalism is applied to describe the relaxation processes in the frequency domain, where the complex permittivity is defined as follows [22]:

$$\varepsilon^*(f) = \varepsilon_\infty + \frac{\Delta\varepsilon}{\left[1+\left(i\frac{f}{f_{\mathrm{HN}}}\right)^{\beta_{HN}}\right]^{\gamma_{HN}}} \tag{2}$$

The $\Delta\varepsilon$ describes the temperature-dependent intensity of the relaxation and can be determined by the following equation:

$$\Delta\varepsilon = \sum_{i=1}^{k} \frac{1}{\varepsilon_0} g \frac{\mu^2}{k_{\mathrm{B}}T} \frac{N}{V} \tag{3}$$

where ε_0 is the permittivity in the vacuum, T is the temperature, μ is the dipole moment, N/V is the number density of the dipoles involved and g is the Kirkwood–Fröhlich factor. The summation is used to determine the total dielectric strength if a number of different types of dipoles contribute to the relaxation process [22].

Alpha (α), normal mode (n-mode), interfacial relaxations and gamma (γ) relaxations

Figure 8A illustrates the measured frequency dependence of ε' at 100 °C for the unfilled epoxy system. The measured ε' appears to have considerable contributions from charge transport, where the slope on logarithmic axes is − 1 [52]. Similar behaviour can be observed for all other systems; the plots are not included for brevity.

Figure 8a, b depicts the $\varepsilon''_{\mathrm{derived}}$ for all the epoxy systems at 100 °C and 160 °C, respectively. These dielectric spectra reveal three relaxation processes: α, *n*-mode relaxations and interfacial polarisation. All these relaxation processes shift towards higher frequencies with an increase in temperature.

The α relaxation is associated with the cooperative motions of the polymer backbone [53] and is distinctly observed at 100 °C in all the samples at similar frequencies. As expected, no significant changes are observed in terms of α; as mentioned earlier, no T_g variations were observed.

An additional low-frequency process is observed at lower frequencies (unfilled epoxy and SiO_2); this process is associated with the normal mode relaxation process and is attributed to the long-range end-to-end dipole vector along the polymer chain [52]. The n-mode is observed in all samples at 160 °C. Finally, another low-frequency relaxation process enters the observed window at 160 °C and is likely attributed to interfacial polarisation phenomena [12, 54]. A distinct additional interfacial relaxation peak is observed in the SiO_2 filled system which is not observed in the sample filled with h-SiO_2. Two additional interfacial polarisation peaks are observed in the case of SiO_2–SiO_2 filled systems, potentially originating from the polymer–shell interface at higher frequency and core (crystalline)–shell (amorphous) interface at low frequency. At temperatures above 120 °C, additional features are observed, which may be due to the electrode polarisation [52].

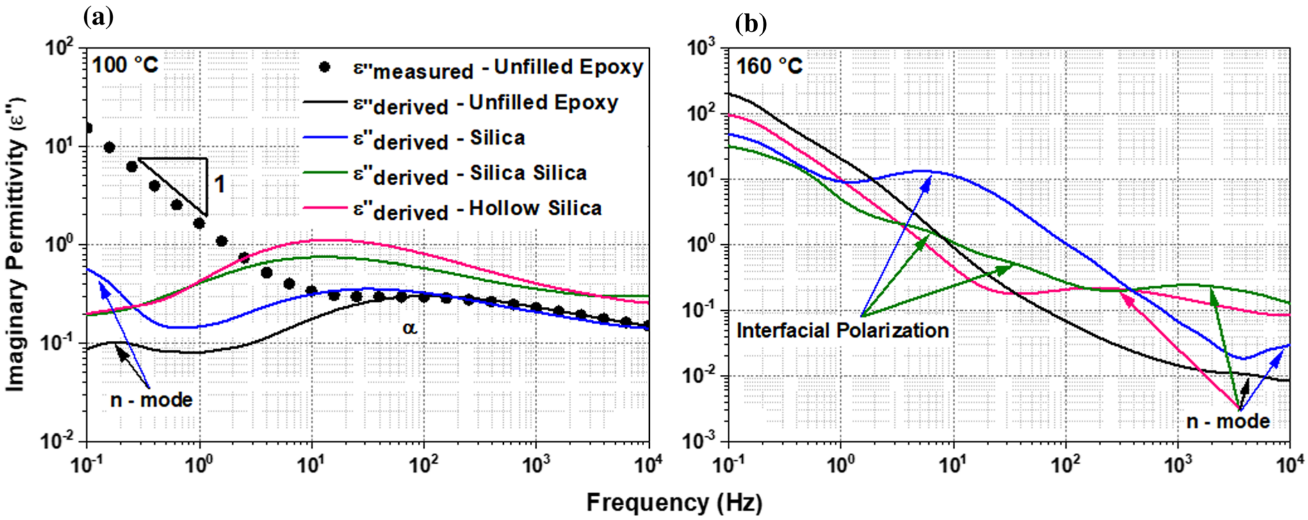

Figure 8 ε'' (measured–unfilled epoxy) and ε'' (derived) dielectric spectra for all the epoxy systems at **a** 100 °C presenting the α relaxation and **b** 160 °C presenting the *n*-mode relaxation and interfacial polarisation phenomena.

The HN deconvolution of the n-mode and interfacial peaks could not be accurately performed to attain any meaningful data as the permittivity of the fillers and that of the host are similar, resulting in closely overlapping peaks. In order to investigate these features, different nanofillers with significant permittivity difference with respect to unfilled epoxy will be studied.

Figure 9a shows the ε'' data acquired at − 130 °C, presenting the γ relaxation [55]. Deconvolution of the spectra at − 150 °C reveals two gamma relaxation peaks in all samples, namely γ_1 at lower frequencies and γ_2 at higher frequencies (illustrated only for h-SiO_2 in Fig. 9b for brevity). In a recent study by Vryonis et al. [22], these two γ peaks are extensively characterised for epoxy resin composites prepared with different stoichiometric ratios. In that study, the γ_1 is attributed to methylene sequences [56, 57] and γ_2 is assigned to the terminal unreacted epoxide groups [58, 59]. Under optimal stoichiometry, that study reported similar behaviour as in the present study for the unfilled epoxy sample. The dielectric strength ($\Delta\varepsilon$) of the unreacted epoxides in all the filled epoxy nanocomposite systems is approximately the same (0.006 ± 0.002) and marginally smaller in unfilled epoxy (0.0004 ± 0.0001). Therefore, along with the T_g and FTIR results, it is conclusive that the degree of cross-linking in all the nanocomposite systems is similar, if not equivalent.

Beta (β) and omega (ω) relaxations

Figure 10 shows ε'' data obtained for all samples between − 70 and − 30 °C, where β relaxation peak can be observed along with the respective HN fitting. The peak progressively moves to high frequencies with increasing temperature. The β relaxation has been extensively studied after being first reported in 1965 by Kaelble [60], initially proposed to be originating from transitions of diglycidyl segments [61]. Depending upon the structure of the investigated systems, it has also been characterised by features claimed to be attributed to: the rotation of phenyl rings [62]; diphenyl propane segments [63]; absorbed moisture [64]; phase transition of fillers [18, 65]; secondary or tertiary amines or increasing molecular lengths [66]. Such features are not universally observed owing to the different possible structural configurations. The widely accepted interpretation of its physical mechanism comes from a study by Dammont and Kwei [67], attributing the relaxation to the motion of flexible hydroxyl-ether segments formed during the curing. Since then, this relaxation is commonly associated with the degree of cross-linking.

Figure 11 shows the ε'' data obtained at − 30 °C, where the deconvolution reveals three relaxations, across different samples, namely β, β' and ω relaxation. In the unfilled epoxy sample, two overlapping relaxation processes are observed, i.e. the onset of β and the β'. Pangrle et al. attributed the β' relaxation to

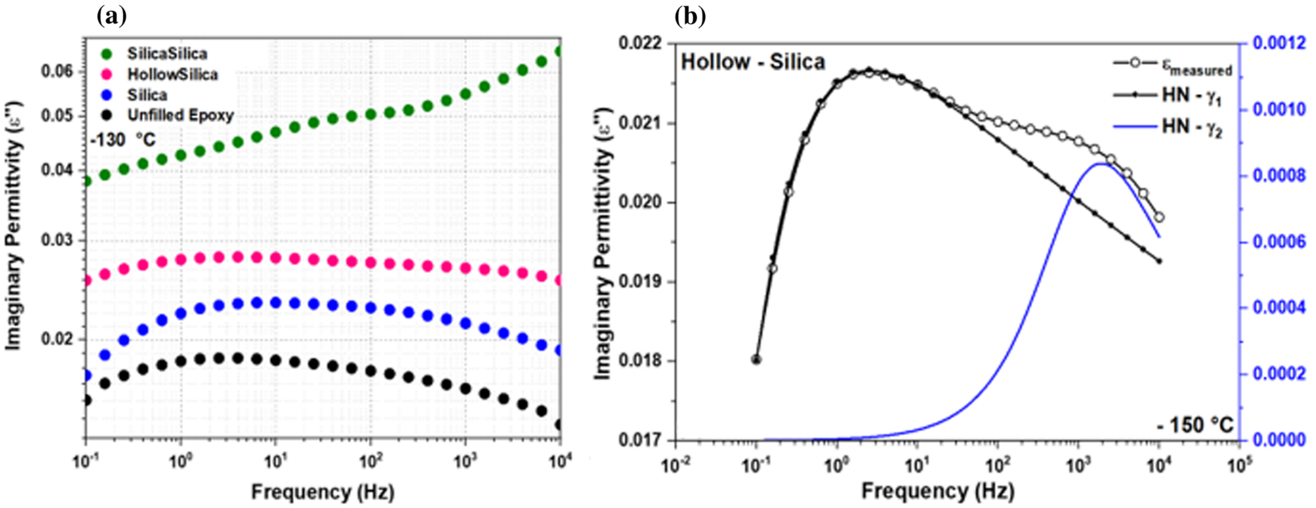

Figure 9 **a** ε'' dielectric spectra presenting the gamma (γ) relaxation for unfilled epoxy, SiO_2 epoxy nanocomposite, SiO_2–SiO_2 epoxy nanocomposite and h-SiO_2 epoxy nanocomposite at a temperature of − 130 °C. **b** Deconvoluted HN gamma peaks for h-SiO_2 at − 150 °C: γ_1 (at lower frequency) and γ_2 (at higher frequency).

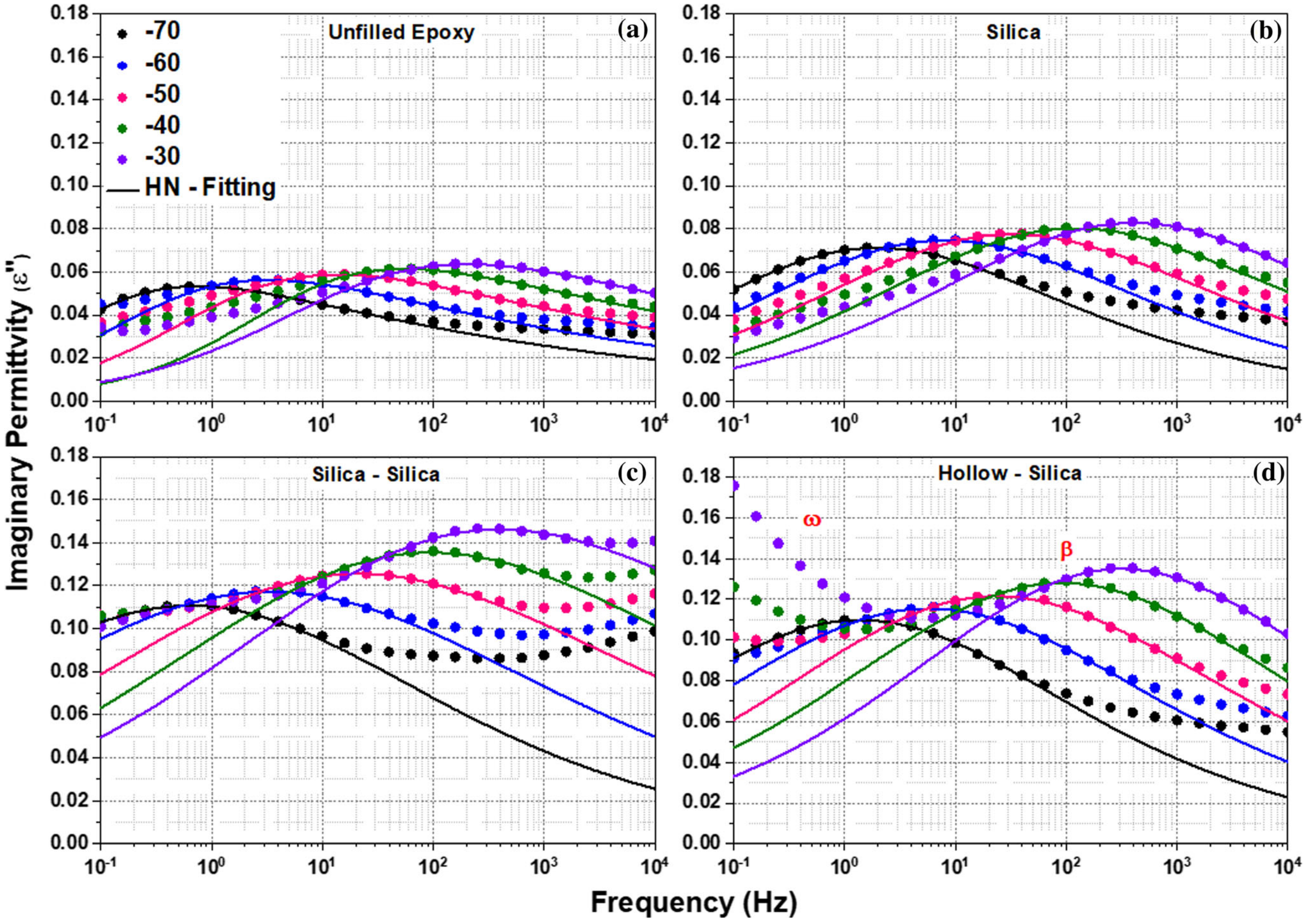

Figure 10 ε'' dielectric spectra presenting the beta (β) relaxation for **a** unfilled epoxy, **b** SiO_2 epoxy nanocomposite, **c** SiO_2–SiO_2 epoxy nanocomposite and **d** h-SiO_2 epoxy nanocomposite for a temperature range of − 70 to − 30 °C along with their corresponding Havriliak–Negami fitting curves.

the cross-link junctions [68], such as the diethylene ether polar groups in nodular domains with higher cross-link density. The diethylene ether groups are produced during the curing reaction as part of the etherification reaction [69]. Alternatively, a recent interpretation related such effects to structural alterations caused by the dehydration reaction (during post-curing at elevated temperatures) leading to the formation of C=C backbone bonds [70]. A similar β' relaxation is observed in SiO_2 filled sample. The peak is broader and stronger in SiO_2–SiO_2 and h-SiO_2. The β' relaxation shows no correlation with any particular dipolar group in this study and appears to be an arbitrary feature possibly arising as a consequence of post-curing, as mentioned above. Deconvoluted β′ modes of the unfilled-, SiO_2- and SiO_2–SiO_2-filled epoxies can be seen in Fig. 11a–c, respectively.

In the SiO_2–SiO_2 filled, as well as h-SiO_2 samples, an additional peak (ω, omega) is observed (Fig. 11c, d). Pangrle et al. [68] attributed the origins of a similar process to the distribution of molecular chain segments and preferential absorption of moisture in low-density cross-link regions. Keenan et al. [64] reported a transition largely affected by moisture, called ω relaxation. The ω relaxation in that study was observed in DMA thermographs, ascribed to a bound nature of water molecules in form of hydrogen bonds with the host polymer. However, such is not entirely the case in our nanocomposite systems as it is observed only as a polarisation phenomenon which is highlighted by the fact that the ω relaxation peak, here, is observed only in dielectric spectra and not in the DMA thermographs (Fig. 12a). A detailed investigation of DMA measurements is beyond the scope of present study and needs a separate study with in-depth analysis. Therefore, for brevity only the DMA thermograph for h-SiO_2 is presented. The key take-away here is that the epoxy nanocomposite sample

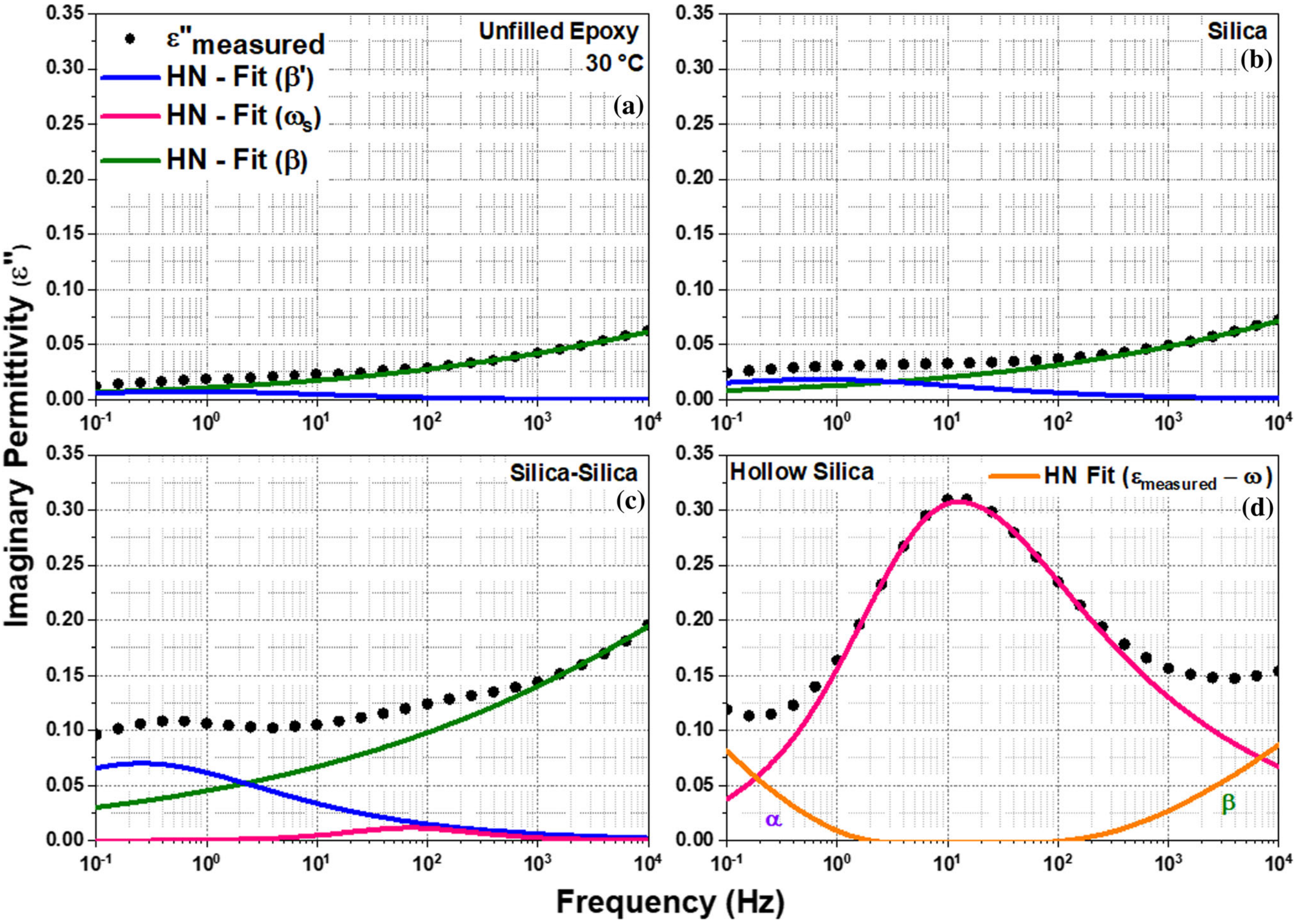

Figure 11 ε'' dielectric spectra presenting the deconvoluted beta (β), beta' (β'), omega (ω) and alpha (α) relaxations for **a** unfilled epoxy, **b** SiO_2 epoxy nanocomposite, **c** SiO_2–SiO_2 epoxy nanocomposite and **d** h-SiO_2 epoxy nanocomposite for a temperature range of 30 °C along with their corresponding HN fitting curves.

filled with h-SiO_2, having the highest concentration of silanols, does not show a corresponding so-called omega (ω) peak in DMA thermograph as is observed in the BDS, similar to all other samples.

Unlike the previous studies, we assume that the ω relaxation, here, is attributed to hydrogen bonding interactions between the nanofillers and the polymer host, as opposed to hydrogen bonding with water molecules, which aligns well with our FTIR results. Since the ω relaxation is located nearby the β relaxation in every case, it is assumed that the hydrogen bonding interactions occur between the silica surface silanols (Si_{OH}) and the epoxy host's hydroxyl-ether segments. The degree of cross-linking is the same in all samples; therefore, the concentration of hydroxyl ethers is also equivalent. Therefore, the $\Delta\varepsilon$ of ω relaxation is proportional to the concentration of Si_{OH}. As a consequence, SiO_2 with the lowest concentration of Si_{OH} results in the weakest ω relaxation. As Si_{OH} concentration increases in the SiO_2–SiO_2 particles, the strength of ω relaxation also increases and a related peak can be observed distinctly after deconvolution. The h-SiO_2 nanoparticles with a completely amorphous structure and the highest concentration of Si_{OH} result in the strongest ω relaxation peak that is largely segregated from the β relaxation and is visible even without peak deconvolution. Figure 12b visually illustrates the effect of overlapping of the ω and β relaxation via HN deconvolution.

Figure 13a presents the temperature variation of Δε for the three relaxations, and Fig. 13b illustrates their corresponding Arrhenius plots. The respective

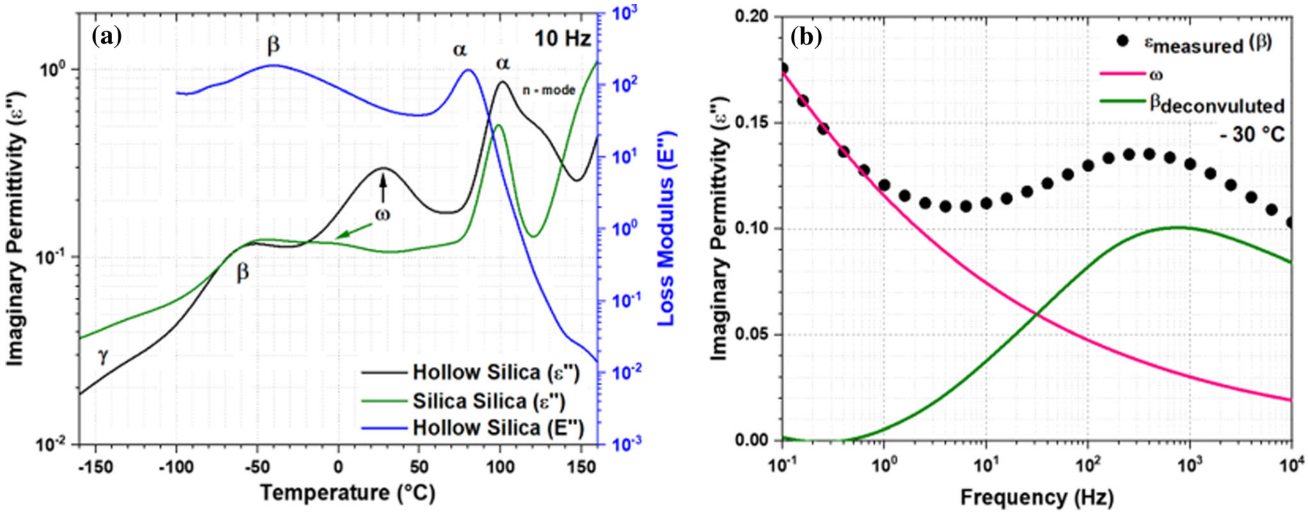

Figure 12 **a** Plot for temperature variation of ε'' at 10 Hz for h-SiO_2 and SiO_2–SiO_2 illustrating the overlapping and segregated nature of ω relaxation in case of SiO_2–SiO_2 and h-SiO_2, respectively, along with a plot of variation of loss modulus (E'') with respect to temperature from DMA for h-SiO_2 filled epoxy nanocomposite and **b** Deconvoluted β and ω relaxation peaks illustrating that the strength of the β relaxation is heavily affected by the ω peak in h-SiO_2.

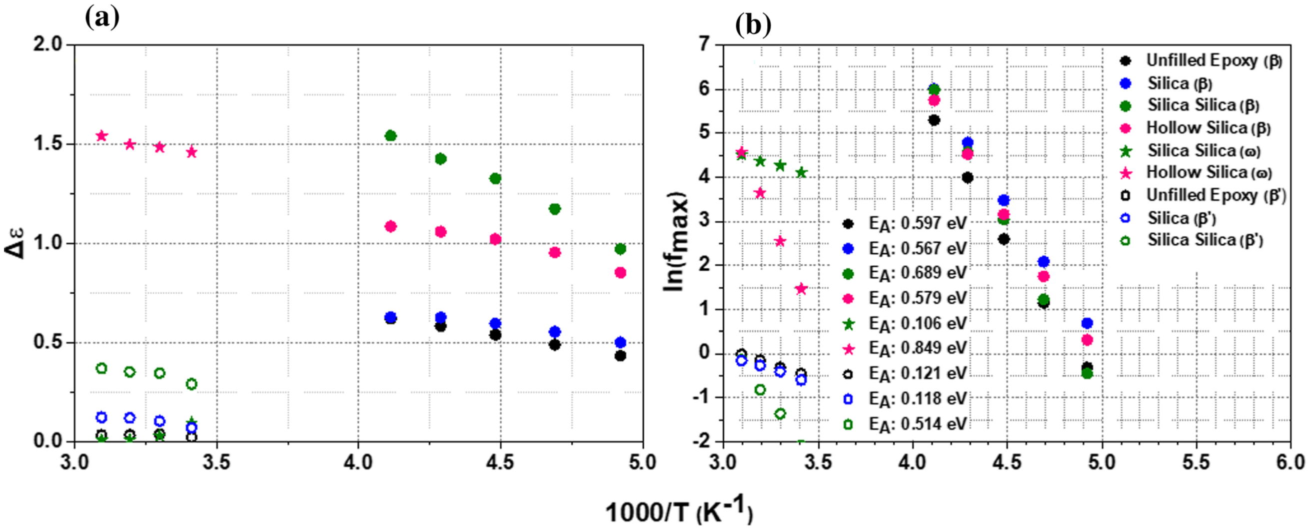

Figure 13 Dielectric data pertaining to the β, β' and ω relaxations for all the systems: **a** temperature variation of $\Delta\varepsilon$ and **b** loss peak position as a function of frequency and temperature (Arrhenius plot).

activation energies could be calculated from the Arrhenius equation as follows [22]:

$$f_{max} = f_0 e^{-\frac{E_A}{k_B T}} \quad (4)$$

where f_{max} is the peak location, f_0 is the pre-exponential factor, k_B is the Boltzmann constant and E_A is the activation energy of the relaxation. In Fig. 13a, it can be observed that the $\Delta\varepsilon$ of β relaxation increases with increasing temperature. This behaviour is similar to and in line with various published studies [22]. In Fig. 13b, the Arrhenius behaviour of β relaxation in the h-SiO_2 sample is parallel to its ω relaxation which suggests these mechanisms involve a similar dipole type (hydroxyl-ether groups). However, this is only observed in case of h-SiO_2 filled epoxy sample. This is most likely due to the significant difference in concertation of the hydroxyl-ether groups between h-SiO_2-, SiO_2–SiO_2- and SiO_2-filled samples. Therefore, in case of SiO_2-filled epoxy sample having the least concentration of these groups, deconvolution of the peaks at multiple temperatures to calculate the activation energy was not possible and not shown.

Conclusion

Three types of epoxy nanocomposites with different silica architectures, i.e. SiO_2, SiO_2–SiO_2 (core shell structures) and h-SiO_2 (hollow structure), were investigated in this study. Significant changes are observed in the temperature range of − 90 to 50 °C, where the deconvolution reveals three relaxations β, β' and ω. The β relaxation is attributed to the hydroxyl-ether groups formed during curing, β' is assigned to structural alterations caused at post-curing temperatures, and ω is attributed to the hydrogen bond interactions between the silanol groups on the silica surfaces and the hydroxyl-ether groups of the host network. The overlapping of the ω with β and β' increases their $\Delta\varepsilon$ and activation energy (− 70 to − 30 °C), as observed in the SiO_2–SiO_2 sample. In the physical sense, the formation of hydrogen bonds increases the amount of energy required to overcome the motion energy barrier. The strength of ω relaxation increases with an increase in Si–OH concentration and also gradually segregates from β. The h-SiO_2 sample with the highest concentration displays completely segregated β and ω peaks. As the Si–OH concentration increases with amorphous content, the FTIR absorbance band intensity of Si–O–Si also increases; this is due to the formation of hydrogen bonds resulting in a dipole change. The ω relaxation is not observed in DMA results and only appears in the dielectric spectra, confirming it as a polarisation phenomenon. Two interfacial polarisation peaks are reported for SiO_2–SiO_2 attributed to be originating from the two interfaces, core–shell and shell–polymer.

Acknowledgements

The research work was performed within the K-Project 'PolyTherm' at the Polymer Competence Centre Leoben GmbH (PCCL, Austria) within the framework of the COMET-program of the Federal Ministry for Transport, Innovation and Technology and the Federal Ministry for Digital and Economic Affairs with contributions by scientific partners and company partners. Funding is provided by the Austrian Government and the State Government of Styria (Österreichische Forschungsförderungsgesellschaft—Grant No. 862835). Authors would also like to thank Professor Michael Feuchter at the Department of Polymer Engineering in Montanuniversitaet Leoben for his help in performing the DMA measurements.

Declarations

Conflict of interest The authors declare that they have no conflict of interest.

References

[1] Liu Y-L, Hsu C-Y, Wei W-L, Jeng R-J (2003) Preparation and thermal properties of epoxy-silica nanocomposites from nanoscale colloidal silica. Polymer 44(18):5159–5167. https://doi.org/10.1016/S0032-3861(03)00519-6

[2] Galpaya D, Wang M, George G, Motta N, Waclawik E, Yan C (2014) Preparation of graphene oxide/epoxy nanocomposites with significantly improved mechanical properties. J Appl Phys 116(5):053518. https://doi.org/10.1063/1.4892089

[3] Li H, Liu F, Tian H, Wang C, Guo Z, Liu P, Peng Z, Wang Q (2018) Synergetic enhancement of mechanical and electrical strength in epoxy/silica nanocomposites via chemically-bonded interface. Compos Sci Technol 167:539–546. https://doi.org/10.1016/j.compscitech.2018.08.047

[4] Tessema A, Zhao D, Moll J, Xu S, Yang R, Li C, Kumar SK, Kidane A (2017) Effect of filler loading, geometry, dispersion and temperature on thermal conductivity of polymer nanocomposites. Polym Test 57:101–106. https://doi.org/10.1016/j.polymertesting.2016.11.015

[5] Qiang D, Wang Y, Wang X, Chen G, Andritsch T (2019) The effect of filler loading ratios and moisture on DC conductivity and space charge behaviour of SiO2 and hBN filled epoxy nanocomposites. J Phys D Appl Phys 52(39):395502. https://doi.org/10.1088/1361-6463/ab2d5b

[6] Miyagawa H, Drzal LT (2004) The effect of chemical modification on the fracture toughness of montmorillonite clay/epoxy nanocomposites. J Adhes Sci Technol 18(13):1571–1588. https://doi.org/10.1163/1568561042411204

[7] Yu Z-Q, You S-L, Yang Z-G, Baier H (2011) Effect of surface functional modification of nano-alumina particles on thermal and mechanical properties of epoxy nanocomposites. Adv Compos Mater 20(5):487–502. https://doi.org/10.1163/092430411X579104

[8] Lewis TJ (1994) Nanometric dielectrics. IEEE Trans Dielectr Electr Insul 1(5):812–825. https://doi.org/10.1109/94.326653

[9] Raetzke S, Kindersberger J (2006) The effect of interphase structures in nanodielectrics. IEEJ Trans Fundam Mater 126:1044–1049

[10] Tanaka T, Kozako M, Fuse N, Ohki Y (2005) Proposal of a multi-core model for polymer nanocomposite dielectrics. IEEE Trans Dielectr Electr Insul 12(4):669–681. https://doi.org/10.1109/TDEI.2005.1511092

[11] Tsagaropoulos G, Eisenberg A (1995) Dynamic mechanical study of the factors affecting the two glass transition behavior of filled polymers. Similarities and differences with random ionomers. Macromolecules 28(18):6067–6077. https://doi.org/10.1021/ma00122a011

[12] Singha S, Thomas MJ (2008) Dielectric properties of epoxy nanocomposites. IEEE Trans Dielectr Electr Insul 15(1):12–23. https://doi.org/10.1109/T-DEI.2008.4446732

[13] Nelson JK, Fothergill JC (2004) Internal charge behaviour of nanocomposites. Nanotechnology 15(5):586–595. https://doi.org/10.1088/0957-4484/15/5/032

[14] Chen Y-F, Lee C-Y, Yeng M-Y, Chiu H-T (2003) The effect of calcination temperature on the crystallinity of TiO2 nanopowders. J Cryst Growth 247(3):363–370. https://doi.org/10.1016/S0022-0248(02)01938-3

[15] Stöber W, Fink A, Bohn E (1968) Controlled growth of monodisperse silica spheres in the micron size range. J Colloid Interface Sci 26(1):62–69. https://doi.org/10.1016/0021-9797(68)90272-5

[16] Chaudhary S, Andritsch T, Vaughan AS (2020) Effect of nanoparticle volume and surface characteristics on the bulk properties of epoxy nanocomposite. In: 2020 IEEE 3rd international conference on dielectrics (ICD), 5–31 July 2020, pp 269–272. https://doi.org/10.1109/ICD46958.2020.9341845

[17] Takai C, Imabeppu H, Fuji M (2015) Synthesis of hollow silica nanoparticles using poly (acrylic acid)-3,3′-diaminodipropylamine template. Colloids Surf A 483:81–86. https://doi.org/10.1016/j.colsurfa.2015.07.022

[18] Wan Y, Yu S-H (2008) Polyelectrolyte controlled large-scale synthesis of hollow silica spheres with tunable sizes and wall thicknesses. J Phys Chem C 112(10):3641–3647. https://doi.org/10.1021/jp710990b

[19] Saeedi IA, Vaughan AS, Andritsch T, Virtanen S (2016) The effect of curing conditions on the electrical properties of an epoxy resin. In: 2016 IEEE conference on electrical insulation and dielectric phenomena (CEIDP), 16–19 Oct. 2016, pp 461–464. https://doi.org/10.1109/CEIDP.2016.7785649

[20] Chaudhary S, Andritsch T, Vaughan AS (2019) Effect of core–shell particles on the dielectric properties of epoxy nanocomposites. In: 2019 IEEE conference on electrical insulation and dielectric phenomena (CEIDP), 20–23 Oct. 2019, pp 729–732. https://doi.org/10.1109/CEIDP47102.2019.9009643

[21] Chaudhary S, Vryonis O, Vaughan AS, Andritsch T (2021) Dielectric response in epoxy nanocomposites incorporating various nano-silica architectures. In: 2021 IEEE conference on electrical insulation and dielectric phenomena (CEIDP), 12–15 Dec. 2021, pp 57–60. https://doi.org/10.1109/CEIDP50766.2021.9705316

[22] Vryonis O, Riarh S, Andritsch T, Vaughan AS (2021) Stoichiometry and molecular dynamics of anhydride-cured epoxy resin incorporating octa-glycidyl POSS Co-monomer. Polymer 213:123312. https://doi.org/10.1016/j.polymer.2020.123312

[23] Koopman M, Gouadec G, Carlisle K, Chawla KK, Gladysz G (2004) Compression testing of hollow microspheres (microballoons) to obtain mechanical properties. Scr Mater 50(5):593–596. https://doi.org/10.1016/j.scriptamat.2003.11.031

[24] Buyuknalcaci FN, Polat Y, Negawo TA, Döner E, Alam MS, Hamouda T, Kilic A (2018) Carbon nanotube-based nanocomposites for wind turbine applications. In: Jawaid M, Khan MM (eds) Polymer-based nanocomposites for energy and environmental applications. Woodhead Publishing, Sawston, pp 635–661

[25] Wiberg E, Wiberg N, Holleman AF (2001) Inorganic chemistry. Academic Press, Berlin

[26] Kirfel A, Krane H-G, Blaha P, Schwarz K, Lippmann T (2001) Electron-density distribution in stishovite, SiO2: a new high-energy synchrotron-radiation study. Acta Crystallogr A 57(6):663–677. https://doi.org/10.1107/S0108767301010698

[27] Ding Y, Chu X, Hong X, Zou P, Liu Y (2012) The infrared fingerprint signals of silica nanoparticles and its application in immunoassay. Appl Phys Lett 100(1):013701. https://doi.org/10.1063/1.3673549

[28] Imam Supardi ZA, Nisa Z, Kusumawati DH, Putri NP, Taufiq A, Hidayat N (2018) Phase transition of SiO2 nanoparticles prepared from natural sand: the calcination temperature effect. J Phys Conf Ser 1093:012025. https://doi.org/10.1088/1742-6596/1093/1/012025

[29] Rudin A, Choi P (2013) Chapter 4—Mechanical properties of polymer solids and liquids. In: Rudin A, Choi P (eds) The elements of polymer science & engineering, 3rd edn. Academic Press, Boston, pp 149–229. https://doi.org/10.1016/B978-0-12-382178-2.00004-3

[30] Gibbs GV, Hill FC, Boisen MB, Downs RT (1998) Power law relationships between bond length, bond strength and electron density distributions. Phys Chem Miner 25(8):585–590. https://doi.org/10.1007/s002690050151

[31] Linnett JW, Reuben BG (1959) Changes in molecular dipole moments on distortion. Trans Faraday Soc 55:510–514. https://doi.org/10.1039/TF9595500510

[32] Marco LD, Thämer M, Reppert M, Tokmakoff A (2014) Direct observation of intermolecular interactions mediated by hydrogen bonding. J Chem Phys 141(3):034502. https://doi.org/10.1063/1.4885145

[33] Nhan NT, Trang GTT, Iitaka T, Hong NV (2019) Crystallization of amorphous silica under compression. Can J Phys 97(10):1133–1139. https://doi.org/10.1139/cjp-2018-0432

[34] Fornaro T, Burini D, Biczysko M, Barone V (2015) Hydrogen-bonding effects on infrared spectra from anharmonic computations: uracil-water complexes and uracil dimers. J Phys Chem A 119(18):4224–4236. https://doi.org/10.1021/acs.jpca.5b01561

[35] Pliskin WA (1977) Comparison of properties of dielectric films deposited by various methods. J Vac Sci Technol 14(5):1064–1081. https://doi.org/10.1116/1.569413

[36] Ponton S, Dhainaut F, Vergnes H, Samelor D, Sadowski D, Rouessac V, Lecoq H, Sauvage T, Caussat B, Vahlas C (2019) Investigation of the densification mechanisms and corrosion resistance of amorphous silica films. J Non-Cryst Solids 515:34–41. https://doi.org/10.1016/j.jnoncrysol.2019.04.005

[37] Hattori H, Arudra P, Abdalla A, Aitani AM, Al-Khattaf SS (2020) Infrared study of silanol groups on dealuminated high silica MFI zeolite to correlate different types of silanol groups with activity for conversion of 1-butene to propene. Catal Lett 150(3):771–780. https://doi.org/10.1007/s10562-019-02972-8

[38] Wilhelm S, Kind M (2015) Influence of pH, temperature and sample size on natural and enforced syneresis of precipitated silica. Polymers 7(12):2504–2521

[39] Mackie DM, Jahnke JP, Benyamin MS, Sumner JJ (2016) Simple, fast, and accurate methodology for quantitative analysis using Fourier transform infrared spectroscopy, with bio-hybrid fuel cell examples. MethodsX 3:128–138. https://doi.org/10.1016/j.mex.2016.02.002

[40] Spallino L, Vaccaro L, Sciortino L, Agnello S, Buscarino G, Cannas M, Gelardi FM (2014) Visible-ultraviolet vibronic emission of silica nanoparticles. Phys Chem Chem Phys 16(40):22028–22034. https://doi.org/10.1039/C4CP02995J

[41] Cholake S, Mada M, Singh R, Bai Y, Zhao X-L, Rizkalla S, Bandyopadhyay S (2014) Quantitative analysis of curing mechanisms of epoxy resin by mid- and near- Fourier transform infra red spectroscopy. Def Sci J 64:314–321. https://doi.org/10.14429/dsj.64.7326

[42] Finzel MC, Delong J, Hawley MC (1995) Effect of stoichiometry and diffusion on an epoxy/amine reaction mechanism. J Polym Sci, Part A: Polym Chem 33(4):673–689. https://doi.org/10.1002/pola.1995.080330409

[43] Gonzalez M, Cabanelas J, Baselga J (2012) Applications of FTIR on epoxy resins-identification, monitoring the curing process, phase separation and water uptake. Infrared Spectrosc Mater Sci Eng Technol 2:261–284. https://doi.org/10.5772/36323

[44] Saeedi IA, Andritsch T, Vaughan AS (2019) On the dielectric behavior of amine and anhydride cured epoxy resins modified using multi-terminal epoxy functional network modifier. Polymers 11(8):1271. https://doi.org/10.3390/polym11081271

[45] Dalstein L, Potapova E, Tyrode E (2017) The elusive silica/water interface: isolated silanols under water as revealed by vibrational sum frequency spectroscopy. Phys Chem Chem Phys 19(16):10343–10349. https://doi.org/10.1039/C7CP01507K

[46] Bell JP (1970) Structure of a typical amine-cured epoxy resin. J Polym Sci Part A2 Polym Phys 8(3):417–436. https://doi.org/10.1002/pol.1970.160080308

[47] Vryonis O, Virtanen STH, Andritsch T, Vaughan AS, Lewin PL (2019) Understanding the cross-linking reactions in highly oxidized graphene/epoxy nanocomposite systems. J Mater Sci 54(4):3035–3051. https://doi.org/10.1007/s10853-018-3076-8

[48] Pogany GA (1970) The α relaxation in epoxy resins. Eur Polym J 6(2):343–353. https://doi.org/10.1016/0014-3057(70)90167-9

[49] Saeedi IA, Vaughan AS, Andritsch T (2016) Change in the electrical properties due to modification of the epoxy network structure using reactive diluents. In: 2016 IEEE conference on electrical insulation and dielectric phenomena (CEIDP), 16–19 Oct. 2016, pp 663–666. https://doi.org/10.1109/CEIDP.2016.7785651

[50] Chang TD, Carr SH, Brittain JO (1982) Studies of epoxy resin systems: Part B: effect of crosslinking on the physical properties of an epoxy resin. Polym Eng Sci 22(18):1213–1220. https://doi.org/10.1002/pen.760221807

[51] Arab B, Shokuhfar A, Ebrahimi-Nejad S (2012) Glass transition temperature of cross-linked epoxy polymers: a molecular dynamics study. In: Proceedings of the international conference nanomaterials: applications and properties, 2012. vol 1, no. 1. Sumy State University Publishing, pp 01NDLCN11–01NDLCN11

[52] Ding R, Torres SW, Messman J, Bowen DE, Bowler N (2018) Dynamics of model polycyclic aromatic hydrocarbon compound-epoxy composites: a dielectric study. Polymer 136:6–16. https://doi.org/10.1016/j.polymer.2017.12.035

[53] Hassan MK, Tucker SJ, Abukmail A, Wiggins JS, Mauritz KA (2016) Polymer chain dynamics in epoxy based composites as investigated by broadband dielectric spectroscopy. Arab J Chem 9(2):305–315. https://doi.org/10.1016/j.arabjc.2015.07.016

[54] Mickish DJ (1979) Effects of interfacial polarization and loading factor in dielectric-loss measurements of composites. J Appl Phys 50(9):5923–5929. https://doi.org/10.1063/1.326692

[55] Hirai T, Kline DE (1973) Effects of heat treatment on dynamic mechanical properties of nonstoichiometric, amine-cured epoxy resins. J Appl Polym Sci 17(1):31–44. https://doi.org/10.1002/app.1973.070170103

[56] Charlesworth JM (1988) Effect of crosslink density on the molecular relaxations in diepoxide-diamine network polymers. Part 1. The glassy region. Polym Eng Sci 28(4):221–229. https://doi.org/10.1002/pen.760280405

[57] Kontos G, Soulintzis A, Karahaliou P, Psarras G, Georga S, Krontiras C, Pisanias M (2007) Electrical relaxation dynamics in TiO2-polymer matrix composites. Express Polym Lett 1(12):781–789

[58] Beiner M, Ngai KL (2005) Interrelation between primary and secondary relaxations in polymerizing systems based on epoxy resins. Macromolecules 38(16):7033–7042. https://doi.org/10.1021/ma050384j

[59] Mijović J, Zhang H (2003) Local dynamics and molecular origin of polymer network−water interactions as studied by broadband dielectric relaxation spectroscopy, FTIR, and molecular simulations. Macromolecules 36(4):1279–1288. https://doi.org/10.1021/ma021568q

[60] Kaelble DH (1965) Dynamic and tensile properties of epoxy resins. J Appl Polym Sci 9(4):1213–1225. https://doi.org/10.1002/app.1965.070090403

[61] May CA, Weir FE (1962) Dynamic mechanical properties of epoxy resins. Polym Eng Sci 2(3):207–212. https://doi.org/10.1002/pen.760020306

[62] Chang TD, Carr SH, Brittain JO (1982) Studies of epoxy resin systems: Part A: a study of the origins of the secondary relaxations of epoxy resins by thermally stimulated depolarization. Polym Eng Sci 22(18):1205–1212. https://doi.org/10.1002/pen.760221806

[63] Takahama T, Geil PH (1982) ″Beta″ relaxation behavior of bisphenol-type resins. J Polym Sci Polym Phys Ed 20(11):1979–1986

[64] Keenan JD, Seferis JC, Quinlivan JT (1979) Effects of moisture and stoichiometry on the dynamic mechanical properties of a high-performance structural epoxy. J Appl Polym Sci 24(12):2375–2387. https://doi.org/10.1002/app.1979.070241206

[65] Soulintzis A, Kontos G, Karahaliou P, Psarras GC, Georga SN, Krontiras CA (2009) Dielectric relaxation processes in epoxy resin—ZnO composites. J Polym Sci, Part B: Polym Phys 47(4):445–454. https://doi.org/10.1002/polb.21649

[66] Mangion MBM, Johari GP (1990) Relaxations of thermosets. III. Sub-Tg dielectric relaxations of bisphenol-A-based epoxide cured with different cross-linking agents. J Polym Sci Part B Polym Phys 28(1):71–83. https://doi.org/10.1002/polb.1990.090280106

[67] Dammont FR, Kwei TK (1967) Dynamic mechanical properties of aromatic, aliphatic, and partially fluorinated epoxy resins. J Polym Sci Part A-2 Polym Phys 5(4):761–769. https://doi.org/10.1002/pol.1967.160050411

[68] Pangrle S, Wu CS, Geil PH (1989) Low temperature relaxation of DGEBA epoxy resins: a thermally stimulated discharge current (TSDC) study. Polym Compos 10(3):173–183. https://doi.org/10.1002/pc.750100305

[69] Mijovic J, Wijaya J (1994) Etherification reaction in epoxy-amine systems at high temperature. Polymer 35(12):2683–2686. https://doi.org/10.1016/0032-3861(94)90400-6

[70] Moller JC, Berry RJ, Foster HA (2020) On the nature of epoxy resin post-curing. Polymers 12(2):466